Article

Comparative Study on Microstructure and Corrosion Resistance of Al-Si Alloy Cast from Sand Mold and Binder Jetting Mold

María Ángeles Castro-Sastre [1],*, Cristina García-Cabezón [2] , Ana Isabel Fernández-Abia [1] , Fernando Martín-Pedrosa [2] and Joaquín Barreiro [1]

1   Department of Mechanical, Informatics and Aerospace Engineering, Campus de Vegazana, University of León, 24071 León, Spain; aifera@unileon.es (A.I.F.-A.); jbarg@unileon.es (J.B.)
2   Materials Engineering, E.I.I., Universidad de Valladolid, 47011 Valladolid, Spain; crigar@eii.uva.es (C.G.-C.); fmp@eii.uva.es (F.M.-P.)
*   Correspondence: macass@unileon.es; Tel.: +34-98-72-93-588

Abstract: This investigation is focused on the corrosion evaluation of an as-cast Al-Si alloy, obtained by two different casting methods: traditional sand casting and three-printing casting, using a binder jetted mold. The experimental results are discussed in terms of chemical composition, microstructure, hardness, and corrosion behavior of two different casting parts. The microstructure and composition of the sample before and after the corrosion tests was analyzed using light microscopy (OM), scanning electron microscopy (SEM), and energy-dispersive X-ray spectroscopy (EDX) and X-ray diffraction (DRX). The corrosion of the two processed castings was analyzed using anodic polarization (PA) test and electrochemical impedance spectroscopy (EIS) in an aerated solution of 3.5% by weight NaCl, similar to the seawater environment. After the corrosion process, the samples were analyzed by inductively coupled plasma/optical emission spectrometry (ICP/OES); the composition was used to determine the chloride solution after immersion times. The sample processed by binder jetting mold showed higher corrosion resistance with nobler potentials, lower corrosion densities, higher polarization resistance, and more stable passive layers than the sample processed by sand casting. This improvement of corrosion resistance could be related to the presence of coarse silicon particles, which decrease of cathodic/anodic ratio and the number of micro-galvanic couples, and the lower amount of intermetallic β Al-Fe-Si phase observed in cast alloy solidified in binder jetting mold.

Keywords: binder jetting; sand casting; aluminum alloy; microstructure; corrosion

1. Introduction

Techniques based on layer-by-layer fabrication have expanded enormously over the past two decades due to the availability of a variety of materials (metals, ceramics, polymers, and sands) and post-treatment procedures [1]. These technologies began for the manufacture of prototypes due to the geometric freedom and validation of physical prototypes during the product development cycle, reducing delivery time. [2,3]. However, several sectors (aerospace, automotive, foundry) have included this new technology in their production to make functional parts. In particular, casting industries immediately identified the benefits of additive manufacturing for the production of molds [4]. The ability to make parts layer by layer allows the designer to achieve one-piece molds, integrating sprue, runner, gate, and feeder into the mold design, and these unique geometries and complex designs are difficult to achieve through traditional casting processes. In addition, manufacturing time is reduced since the production of patterns, use of tools, and machining processes is avoided [5]. These aspects generate enormous advantages considering that more than 70% of all metal castings are produced by the sand casting process [6]. Moreover, sand consumption can be significantly reduced with the additive manufacturing process, which can be helpful for energy saving and reducing environmental pollution as it allows the selective deposition of an acid catalyst (e.g., furan).

Binder jetting is one of the most suitable additive manufacturing technologies for the manufacture of casting molds. Several studies have focused on improving this process, applied to different materials. Tang et al. [7] optimized the binder jetting process for inkjet printing Ti6Al4V parts with excellent properties. Mariani et al. [8] demonstrated the feasibility of binder jetting technology to print WC–Co parts. This study revealed the importance of the characteristics of the initial powder and its influence on the mechanical properties of the printed parts. Other studies have focused on improving inkjet technology. Cheng et al. [9] investigated the process of driving waveform design for the multi-nozzle piezoelectric printhead. The developed procedure allows reducing the number of experimental tests to find suitable waveform parameters for different 3D printers and new materials. Other studies [10] have focused on improving the roller-type leveling mechanism in order to achieve desired layer thickness, smooth surface, and good color quality. Li et al. [11] conducted a study to solve the jamming problem of the printhead and to improve the dimensional accuracy of binder jetting technology. For this purpose, several water-based binders and gypsum composite powders were prepared, and the optimum binder-powder assembly was then determined through elementary adhesive testing and roller paving testing.

In the bibliography, there are several works focused on validating the advantages of applying additive manufacturing technologies to the manufacture of casting molds. Sneling et al. [12] took advantage of using 3D printed molds to cast parts with complex geometries, such as cellular structures and sandwich panels. In this way, they would avoid joints in the final part that would act as stress concentrators. Walker et al. [13] used binder injection technology to manufacture molds with built-in sensors that allowed monitoring the casting process by recording different parameters (temperature, pressure, humidity, gas chemistry) in different parts of the mold during the casting process.

Despite the advantages of applying additive manufacturing in the foundry industry, the process is not yet ready to completely replace the traditional casting process. A deeper understanding of the properties of printed molds and their effect on the quality of castings is still needed. The quality of castings depends on various factors related to the casting process, as well as the properties of the mold used. With regard to the casting process, it is necessary to consider the rate of heat removal from the metal to the mold, the pouring temperature, and the chemical composition of the starting alloy. Regarding the properties of the mold, it is necessary to know the mechanical properties, the surface finish, and the permeability fundamentally. Most of the studies have focused on studying the properties of printed molds using gypsum powder and sand in order to obtain castings of light alloys such as aluminum. McKenna et al. [14] analyzed the effects of temperature and curing time on the mechanical properties of the printed mold. The authors concluded that due to the loss of volatile compounds, permeability increased with increasing curing time. Vaezi et al. [15] studied the effect of layer thickness on mold properties. They observed that by decreasing the thickness of the layer and increasing the amount of binder added between particles bond, an improvement in tensile strength was achieved, although worse results were produced in the surface quality of the mold. Edwin et al. [16] studied the feasibility of printing plaster molds to produce aluminum metal castings. To improve the mechanical and thermal properties of the mold, they performed post-processing operations such as infiltration. The infiltrated molds had good resistance to heat, although the mold did not have enough mechanical strength to withstand the metallostatic pressure due to the molten metal.

There have been some studies that analyzed the quality of the castings obtained from 3d printed molds but the number of studies is limited. Snelling et al. [17,18] conducted a comparative study using two different materials to produce the 3DP mold—ZCorp's plaster vs. ExOne's silica—in order to obtain A356 aluminum alloy casting. In this study, they focused on analyzing various properties of the casting, including roughness, density, hardness, porosity, and microstructure. They concluded that the material of the mold significantly influences the quality of the final part. Different factors, such as the amount

of binder used to bind the particles of the mold, the grain size, the permeability, and the composition of the mold material, modify the material properties of resultant castings. These properties are related to the microstructural aspects of the final casting matrix (secondary dendrite arm separation, grain size), secondary intermetallic phases (size, morphology, distribution, and quantity), and porosity [19]. Specifically, the microstructure of the Al-Si alloys, the object of study in this article, present in their microstructure a matrix of α-aluminum dendrites as the main component and several phases. Among the phases present are eutectic Si particles, several secondary intermetallic phases such as Al_2Cu, Mg_2Si, and several Fe-bearing phases (AlFeSi, AlFeSiMn). The secondary phases (eutectic Si, Al_2Cu, Mg_2Si, AlFeSi, and AlFeSiMn) provide specific properties to the alloy and can affect the mechanical and corrosion behavior of the material.

Al-Si-Cu alloys are passive materials, however, they show high susceptibility to pitting corrosion in chloride solution; this has been related to the presence of secondary phases because most of these particles are more noble than Al-matrix [20]. These micro- galvanic cells cause the dissolution of the aluminum matrix.

Part of this secondary phase are Si particles. The low solubility of silicon in the aluminum matrix originates the precipitation of Si particles. The size, morphology, and distribution of these particles play an important role in the mechanical and corrosion behavior of Al-Si-Cu alloys [21]. The cathodic behavior of Si within the aluminum-rich matrix acting as an anode results in the formation of micro-galvanic couples that cause localized corrosion [22]. The influence of silicon morphology and its effect on the area ratio in galvanic corrosion has been analyzed by Tahamtan et al. [23]. Thick flake Si particles with sharp edges that increase the cathode/anode ratio greatly increase the density of the corrosion stream [24].

Also, the electrochemical properties of Al-Si-Cu alloys are affected by morphologies, type, and distribution of intermetallic phases that are, in turn, a function of alloy composition and cooling rate [25,26]. Intermetallic particles such as Al_2CuMg, and Mg_2Si, are anodic with respect to the Al matrix and preferably corrode with respect for the surrounding Al matrix [27]. However, the particles of intermetallic phases such as Al_2Cu and especially the iron-rich phases (β-Al-Fe-Si and α-Al-Fe-Mn-Si) are mostly cathodic to the Al and cause the dissolution of surrounding eutectic Al matrix adjacent to these intermetallic phases [28]. The iron content determines the type and morphology of these iron-rich intermetallic phases. The plate shape phase, such as $βAl_5FeSi$, is the most abundant, and the greater the amount of iron, the longer and wider the needles are. This phase is very hard and fragile and induces a high susceptibility to localized corrosion. The presence of manganese favors the "Chinese script" form, such as $αAl_{15}(Fe,Mn)_3Si_2$, which improves corrosion resistance compared with those that are manganese-free [29–31].

The studies at the microstructural level, mechanical properties and corrosion behavior of Al-Si alloys produced by the traditional sand casting process are known. However, little information on these aspects has been studied for castings using molds fabricated by additive manufacturing technology. This work aims to focus on this gap to investigate the microstructure and corrosion behavior of the AlSiCu alloy. For this purpose, the alloys were solidified in traditional sand molds and binder jetting molds.

2. Materials and Methods

2.1. Materials and Molds Manufacturing

For this study, the aluminum alloy Al-Si-Cu (EN-AC 4600) was used. The chemical composition was analyzed by optical emission spectroscopy (OES), and the results are shown in Table 1.

Table 1. Alloy composition in wt. (%).

Si	Fe	Cu	Mn	Mg	Zn	Ni	Cr	Pb	Sn	Ti	Bi	Cd	Co	V	Zr	Al
9.53	1.1	2.05	0.21	0.09	0.9	0.07	0.067	0.04	0.0115	0.08	0.045	0.0006	0.001	0.008	0.008	Bal

The metal pouring conditions were the same for both molds. The aluminum smelting was carried out in a Hobersal PR/400 (Hobersal, Barcelona, Spain) furnace at 770 °C, and the pouring temperature was 750 °C.

The material used to print the binder jetting mold was a commercial powder plaster, $CaSO_4.1/2H_2O$ (VisiJet PXL Core, from 3DSystems, Rock Hill, SC, USA) with a purity of 80–90%, according to the manufacturer and a commercial binder solution (VisiJet PXL Clear) based on water with 2% Pyrrolidone. The characterization of the powder and the binder were carried out by the authors in a previous work [32]. The mold was manufactured using binder jetting technology with a Project CJP 660Pro machine (3D Systems, Rock Hill, SC, USA). Binder Jetting technology is a powder-based process that uses a liquid binder to selectively bind the powder particles that are spread on a work platform. This process is repeated layer by layer until the part is completed according to the CAD design.

To manufacture the sand casting mold, commercial silica sand (Petrobond) was used. A pattern, including the part and filling system, was manufactured by fused deposition modeling (FDM) technology, using Ultimaker 2+ machine (Ultimaker B.V., Utrecht, Dutch). Figure 1 shows the geometry of the part and the methodology used for the manufacture of both molds, obtaining the casting parts, and metallographic and corrosion study. The part has a rounded geometry with a sufficient area-volume ratio to analyze changes in the internal structure due to heat transfer and cooling rate.
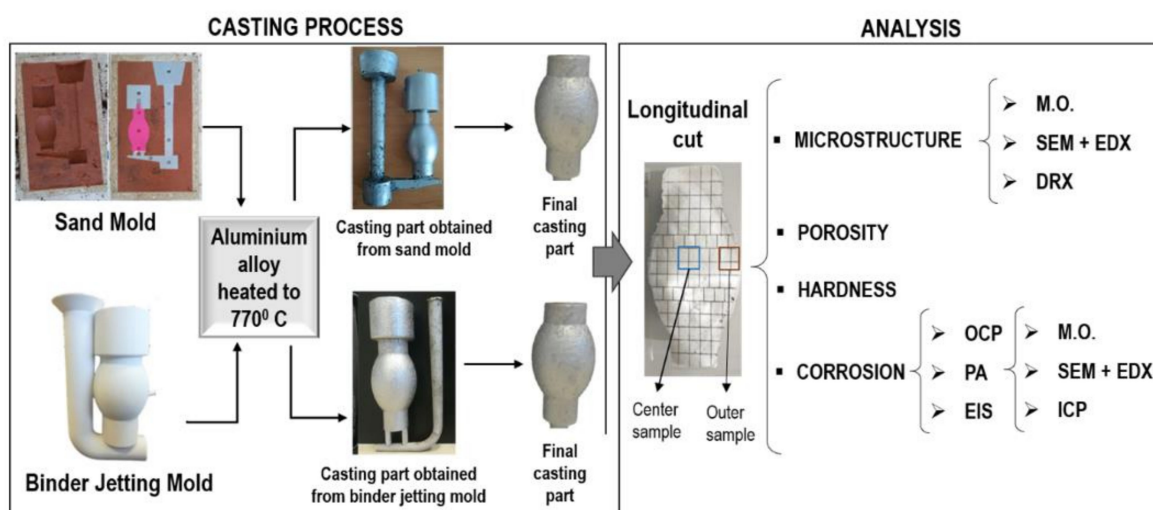

Figure 1. The methodology used for the casting process and analysis of the casting samples (metallographic and corrosion study).

2.2. Microstructural Characterization and Porosity

The metallographic study of both castings was carried out. First, the castings were longitudinally cut and then smaller samples were cut from two different zones of the casting parts, the center and the outer zone. The samples obtained were cold encapsulated and polished (as standard). To reveal the microstructure of the samples, the polished specimens were then etched using Keller's reagent (2.5 mL HNO_3; 1.5 mL HCl, 1 mL HF and 95 mL H_2O) for 12 s. Once polished and attacked, the study of different parameters was carried out, resorting to the use of different techniques.

For the microstructure and porosity study, optical and electronic microscopy was used. The images were taken from each sample (center sample and outer sample) corresponding to the castings obtained from both molds (sand mold and binder jetting printed mold). For the porosity study, a total of 30 images were taken with light microscopy (LM) randomly distributed on the surface of each sample, and then ImageJ 2016-0205 software (National Institute of Health, Bethesda, MD, USA) was used to determine the area occupied by the pores.

The morphological and chemical analysis of the phases was carried out by means of secondary electron imaging (SEI) obtained using a JEOL 6480 scanning electron microscope (SEM) (JEOL, Tokyo, Japan), equipped with an energy dispersive X-ray spectroscopy (EDS) technique was used by means of the AZtec (Matsuzawa Seike Co., Ltd., Tokyo, Japan) analysis software. We also used X-ray diffraction analysis (XRD) using a Bruker D8 Discover diffractometer equipped with a Cu anode (=1.5418 Å).

2.3. Microhardness

A microhardness Vickers test was carried out using Matsuzawa MXT70 microdurometer(EG&G Princeton Applied Research, potentiostat, NJ, USA) with a load of 100 g for 30 s. Hardness samples were extracted from the center and outer locations (Figure 1). Indentations were made until at least 10 indentations were acceptable and each hardness value was calculated by taking the average of the ten identations. The microhardness was evaluated as the arithmetical mean value, and standard deviation was determined.

2.4. Corrosion Testing and Samples Characterization

The corrosion resistance of the casting Al-Si-Cu alloy obtained using a binder jetting mold in comparison with traditional sand casting mold, used as reference, was evaluated from three electrochemical methods: open circuit potential (OCP), anodic polarization measurement (PA), and electrochemical impedance spectroscopy (EIS). The electrochemical testings were carried out in a three-electrode cell using a saturated calomel electrode (SCE) as the reference electrode, graphite as the counter-electrode, and the Al-Si-Cu alloy as the working electrode. The potentiostat 273A EG&G PAR (Princeton Applied Research, Princeton, NJ, USA) and the impedance analyzer Solartron SI 1260 (Princeton Applied Research, Princeton, NJ, USA)were used for monitoring the tests. The corrosion tests were carried out in solution with chlorides (3.5% NaCl at 25 °C). The samples were wet ground with SiC abrasive papers, followed by polishing with 1 mm diamond aqueous suspension. All the electrochemical tests were repeated three times.

The open-circuit potential was measured for 3600 s of immersion of samples in the chloride solution. Potentiodynamic anodic potential curves were made following the ASTM G-5 [33]. Once a nearly quasi-stable potential has been reached, the anodic potentiodynamic scan started at 250 mV below VOCP, reaching $1V_{SCE}$, using 50 mV/min as the potential scan rate. The corrosion potential and current densities were obtained through Tafel's analysis. Electrochemical impedance spectroscopy (EIS) was carried out to evaluate the corrosion polarization resistance (RP). Impedance spectra were performed at open circuit potential after a stabilization step in the open circuit during 1800 s with a signal amplitude of 10 mV at OCP and with a frequency range from 10 MHz to 1Hz. Observations by optical microscopy were done on the corroded samples to understand how the mold casting influences the corrosion performance in Al-Si-Cu alloy.

2.5. Inductive Coupling Plasma (ICP) with Optical Emission Spectrophotometer (OES)

In order to know which phases were dissolved after the corrosion process and to keep the piece in the same medium for 14 days, inductive coupling plasma (ICP) with optical emission spectrophotometer (OES) (ICP-OES) was used. The model was Perkin Elmer Optima 2000DV. The samples were measured directly, undiluted. The ICP equipment (Agilent Technologies Australia, Made in Malaysia) was calibrated with the following standards: 0, 0.01, 0.05, 0.1, 0.5, 1, and 10 ppm.

3. Results and Discussion

3.1. Microstructural Characterization of Aluminum Alloy Castings

Figure 2 shows the microstructures solidified in both molds. Figure 2a–f represents the solidified microstructures in a binder jetting mold, while Figure 2g–l represents the solidified microstructures in a sand mold. As can be seen, when comparing these figures, different mold materials produce some changes in the morphology and size of some phases.

Regarding the size of the phases, it is evident that they are much smaller in the parts obtained by sand mold, especially in the outer area of the parts, which could be associated with the higher cooling speed in this area. As for the shape, it can be seen that elongated shapes predominate in the sand mold. However, the phases present in the outer zone of the binder jetting mold appear as thick phases with an irregular geometric and elongated shape in most of the phases. The phases of Si, in these cases, are more elongated.
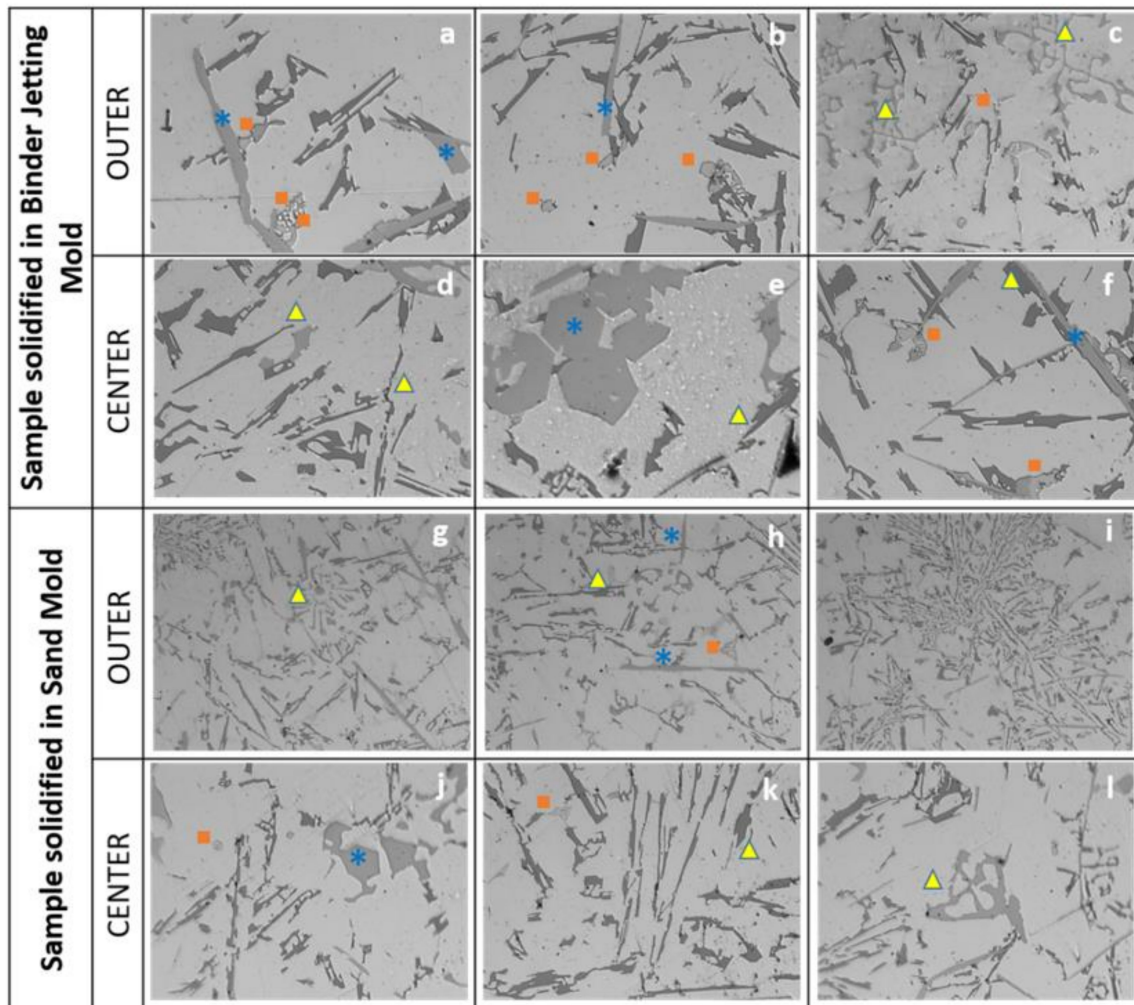

Figure 2. Optical micrographs of the samples: obtained in the outer area (**a**–**c**) from binder jetting mold and (**g**–**i**) from sand mold, and obtained in the center area (**d**–**f**) from binder jetting mold and (**j**–**l**) from sand mold. ∗ Si phase; ■ Al_2Cu phase; △ Al-Fe-Si phase.

It is known that the microstructure in aluminum alloy contains a matrix of α-aluminum dendrites as the main component, which is surrounded by the eutectic Al-Si aggregate and various secondary phases. Among the phases present are eutectic Si particles, several secondary intermetallic phases such as Al_2Cu, Mg_2Si, and several Fe-bearing phases (AlFeSi, AlFeSiMn). In our case, the microstructure that results from the melting in both molds consisted of an aluminum matrix, in which some phase is distributed. Coarse pro-eutectic Si particles (Figure 2e–j) and also Si needles particles (Figure 2b–f,h) can be observed. Iron phases can generally be divided into three different morphologies: polyhedral crystals, Chinese script, or thin platelets. The plate-like phases, such as β-Al_5FeSi, are considered more harmful than script-type phases and polyhedral crystals, such as α-Al_{15}- $(Fe,Mn)_3Si_2$ [29,30,34]. All of them appear in the two castings obtained in both types of molds (Figure 2c–h,k,l). Al_2Cu appears with irregular rounded shapes, most of

them near to the Si and Fe phases, indicating that these phases may act as a nucleation site (Figure 2a–c,f,h,j,k). This phase seems to be mostly found in the cast part obtained in a mold made with Binder Jetting.

Using SEM, it was possible to obtain Secondary Electron Imaging (SE), in order to know the composition of the different phases identified by OM (Figure 2). The results are shown in Figure 3. In this Figure, some images are collected, and one of them corresponds to the image of secondary electrons (SE) of the selected area, five of them to high-resolution X-ray spatial distribution maps corresponding to the elements present in the SE area. Iron is represented by green point density, which patterns distribution mappings is closely correlated with yellow point density corresponding to Mn and in some points with aluminum. This correlation between this element is indicating the presence of Al-Fe-Mn phase. The silicon distribution is not close to any element, so this indicates the presence of eutectic silicon particles.
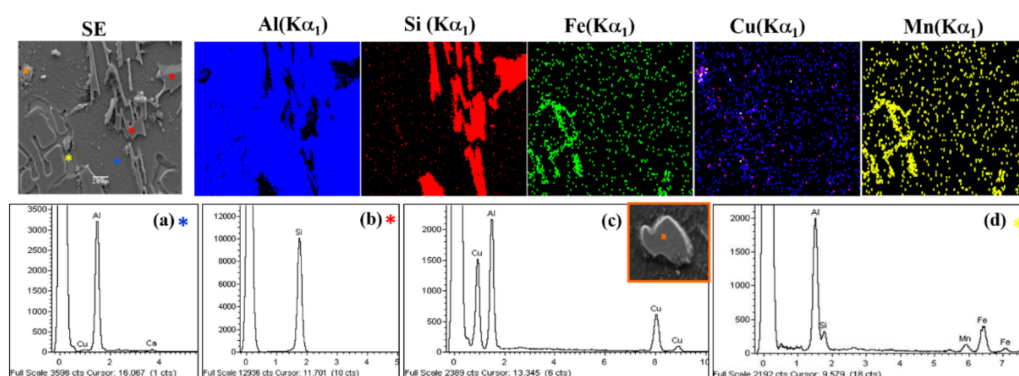

Figure 3. Mapping analysis of an area on the surface of the casting specimen, and 3 (**a**–**d**) X-ray spectra obtained at different points in the area as a function of the distribution of the elements.

The ED X-ray spectrum is derived from different areas on the SE image, depending on the distribution of the elements shown in the X-ray images. This has allowed corroborating the presence of different phases: silicon (Figure 3b), Al_2Cu (Figure 3c), and Al-Fe-Si-Mn (Figure 3d) in that area.

The secondary iron phase (Al-Fe-Mn-Si) appeared in both molds with two different defined morphologies (Figure 4). On the one hand, particles with the shape of Chinese script appeared (Figure 4a), and on the other hand, particles with irregular shapes (Figure 4b).
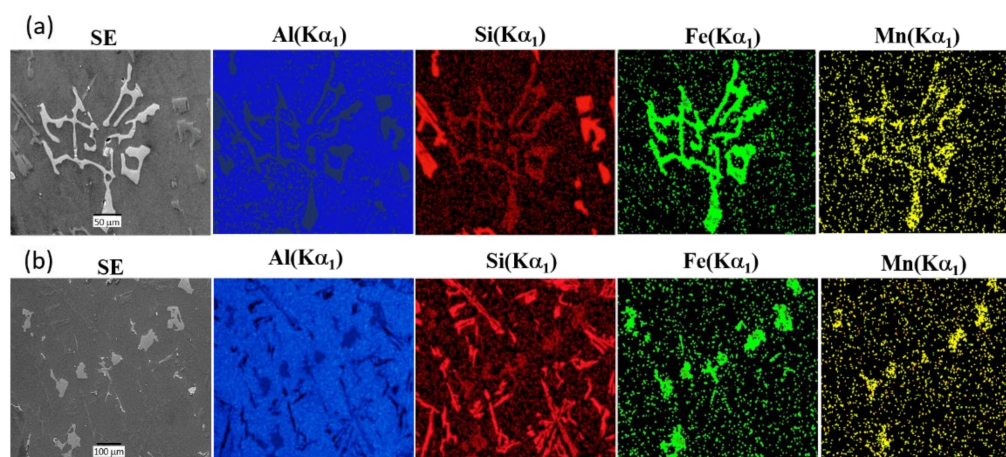

Figure 4. Mapping analysis of two different phases of iron. Chinese script (**a**), and irregular shape (**b**).

Figure 5 and Table 2 show the experimental results of the XRD patterns of the four samples studied (sand mold and binder jetting mold in the outer and central zones). As

it can be observed, the phase proportions vary slightly both in the analyzed position (center-exterior) and when changing the mold. The XRD analysis revealed the presence of Al, and Si eutectic, as the major peaks. In addition, small diffraction peaks of $CuAl_2$ intermetallic phase were detected, which proved that the Cu particles had reacted with the Al matrix-forming $CuAl_2$ intermetallic, as suggested by the EDS analysis. In Figure 5, peaks at ~8°, 44°, 64°, 78°, and 83° correspond to the Bragg planes (111), (200), (220), (311), and (222), respectively, indicating the presence of aluminum. On the other hand, the peaks that appear at ~28°, 48°, 56°, 77°, and 88° indicate the presence of the eutectic Si phase in the Bragg planes (111), (220), (311), (331), and (422). These results are consistent with other investigations of AlSi alloys as well as sintered compounds of these [35–37].
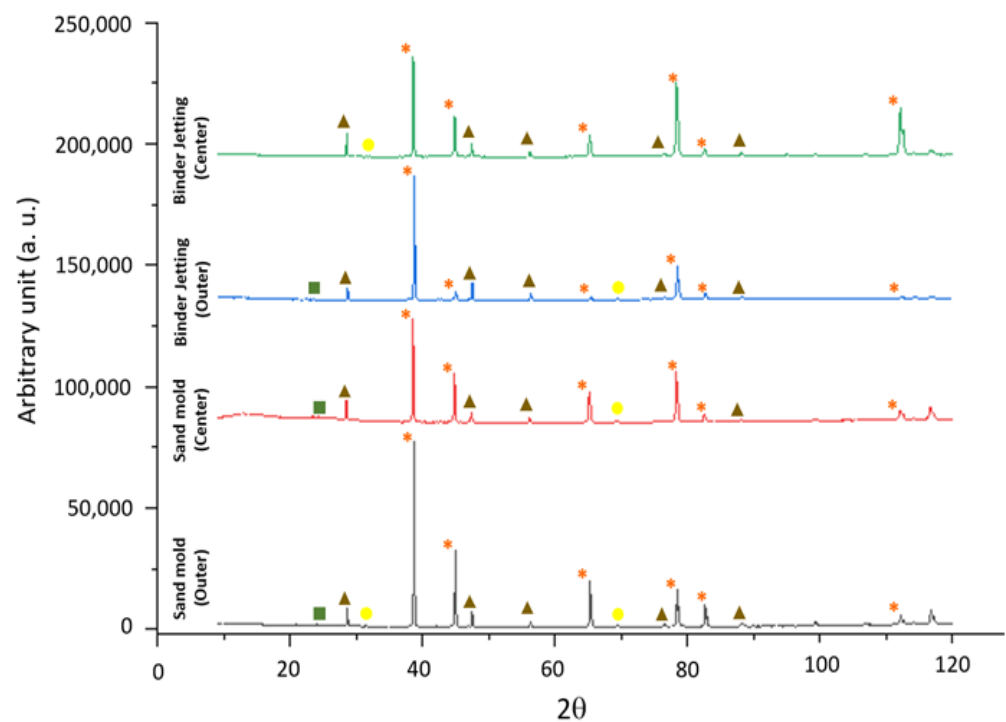

Figure 5. Experimental XRD patterns of the aluminum-silicon alloy processed by sand and binder jetting mold. (∗ Al; ▲ Si; ● Al_2Cu; ■ AlFeMn).

Table 2. Semi-quantitative results for the samples solidifies in both molds (sand mold and binder jetting mold).

Phases	Binder Jetting		Sand Casting	
	Outer	**Center**	**Outer**	**Center**
Al	42	76.1	30.6	80.3
Si	7.6	0.7	5.1	1.4
Al-Fe-Si	28.1	18.4	52.2	12.4
Al_2Cu	10.9	2.6	7.5	2.0
Al-Fe-Mn-Si	11.3	1.4	1.0	2.5
Mg_2Si	2.7	0.8	1.1	1.3

Weaker peaks at approximately 41°, 42°, and 69° corresponding to the (220) and (222) Bragg planes indicating the minority presence of Al_2Cu [38].

The XRD results reveal that the composition of the alloy is similar in both cases, although the content of each phase is different for the binder jetting and sand mold. The results of a semi-quantitative analysis of these samples are shown in Table 2. According to the results, it is possible to conclude that the silicon phase is the majority in the exterior zone for both molds, however, it appears in a greater proportion for samples obtained by

binder jetting mold. In addition, for both molds, the secondary phases predominate in the outer area of the piece, and they are also the majority in binder jetting mold. However, the aluminum phase is predominant for both molds in the central zone, although this phase is the majority in the case of the sand mold.

In addition to the identification of phases and their distribution, in this work, the dendritic size was also determined in both areas of the castings (exterior and center) because it is an important parameter to take into account when evaluating the corrosion behavior.

From the OM micrographs, the secondary dendrite arm separation (SDAS) was measured (Figure 6) and the results are collected in Table 3. In both areas, exterior and center, higher SDAS values for the sample were obtained with the binder jetting mold. From it, it was determined to establish the cooling speeds of the solidified alloys in the two molds and in the two studied areas. For this purpose, Equation (1) was used [39].

$$\log R = -2.5 \log \Lambda s + 4.5 \tag{1}$$

where Λs is the secondary dendrite arm separation (µm) and R is the cooling speed (°C/s).
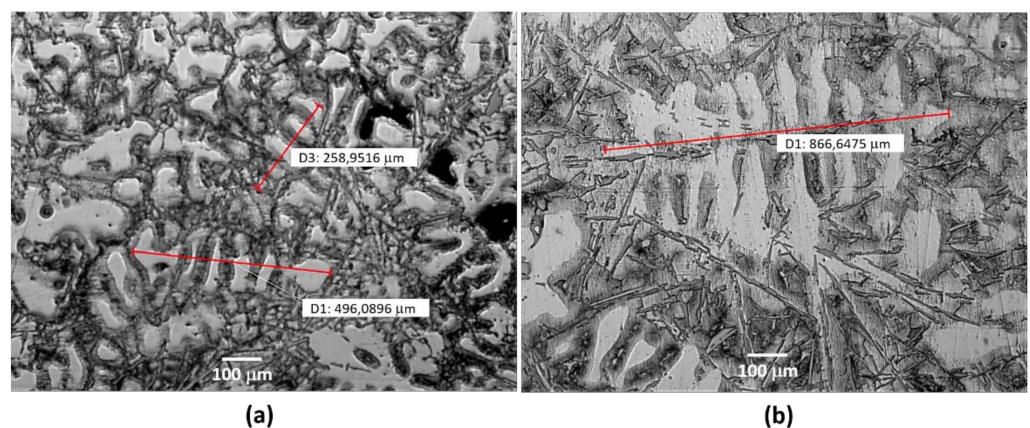

Figure 6. OM micrographs used to evaluate the SDAS (**a**) dendrites solidified in sand mold, and (**b**) dendrites solidified in binder jetting mold.

Table 3. Cooling rates obtained from Equation (1) and the SDAS values.

Parameters	Binder Jetting		Sand Casting	
	Outer	**Center**	**Outer**	**Center**
SDAS (µm)	96.21	120.37	70.62	81.48
Cooling Rate (°C/s)	0.35	0.19	0.75	0.52

Table 3 shows the cooling rates, calculated using Equation (1), taking into account the determined secondary experimental dendrite arm spacing (SDAS). In the investigated alloy, it can be seen that the highest solidification speed occurred in the outer areas of the cast part, according to the lowest value of SDAS.

These compositional and morphological differences observed in the samples analyzed, notably influence the corrosion behavior, as indicated in the following sections.

3.2. Porosity and Hardness Study of Solidified Samples

To analyze porosity, a longitudinal cut was made in the castings, as indicated in Section 2.2. For both cases, sand casting and binder jetting casting, two types of porosity were detected. As can be seen in Figure 7, in both casting processes, the same type of porosity appeared in the samples: (1) spherical pores as a consequence of gas trapping (Figure 7a,c), and (2) dendritic porosity due to the shrinkage that occurs during the solidification process (Figure 7b,d).
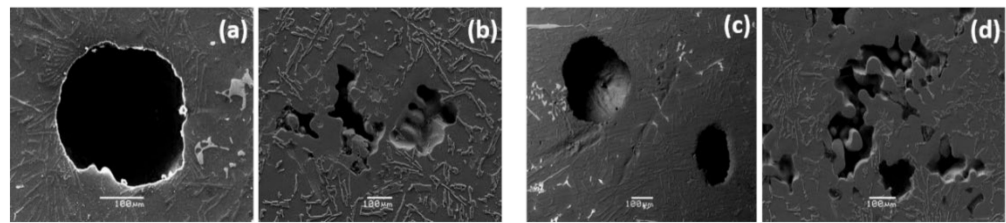
Figure 7. Micrographs obtained by SEM revealing the porosity present in the samples solidified in binder jetting mold (**a**,**b**) and in sand mold (**c**,**d**).

Although the same type of porosity was observed with both processes, it should be noted that the presence of pores due to gas trapping was higher when the sample was obtained from the mold processed by additive manufacturing. This may be because the 3D mold is processed by additive manufacturing; it contains higher moisture, volatile substances, and impurities compared to the traditional mold. This high content of volatile substances means that the castings from the mold processed by 3D Binder Jetting present a slight increase in both the number and the size of the pores.

The porosity percentage on the surface of the casting part was also determined (Table 4). The area occupied by pores was significantly higher in the specimen obtained with binder jetting mold, with this difference being more accused of the center specimen.

Table 4. % Porosity of casting specimens solidified in sand mold and binder jetting mold.

Type of Mold	% Porosity	
	Outer	Center
Sand mold	3.39	3.02
Binder jetting mold	3.68	4.35

The mean Vickers microhardness for all samples are indicated in Table 5. The microhardness values do not present significant differences neither with the type of mold, nor with the region analyzed in the samples.

Table 5. Hardness values of casting specimens: binder jetting and sand casting.

Type of Mold	HV 0.1/30	
	Outer	Center
Sand Mold	65.54	62.86
Binder Jetting Mold	63.26	62.70

3.3. Corrosión Behavior

Al-Si-Cu alloy processed by sand casting and by binder jetting casting corresponding to the central and outer zones were immersed in the 3.5 wt.% NaCl solution at 20 °C during 3600 s and the open circuit potential was recorded, Figure 8a. For both sections and for both casting processes, the potential slightly increased over time, thus, it is indicative of a passive layer formation process on the surface. In all cases, there were notable potential fluctuations that reveal the difficulties of forming a stable passive layer. The potentials are slightly higher for binder jetting casting, indicating that thermodynamically the corrosion resistance is somewhat higher than for sand casting. The differences between the center and outer sections are minimal for both samples.
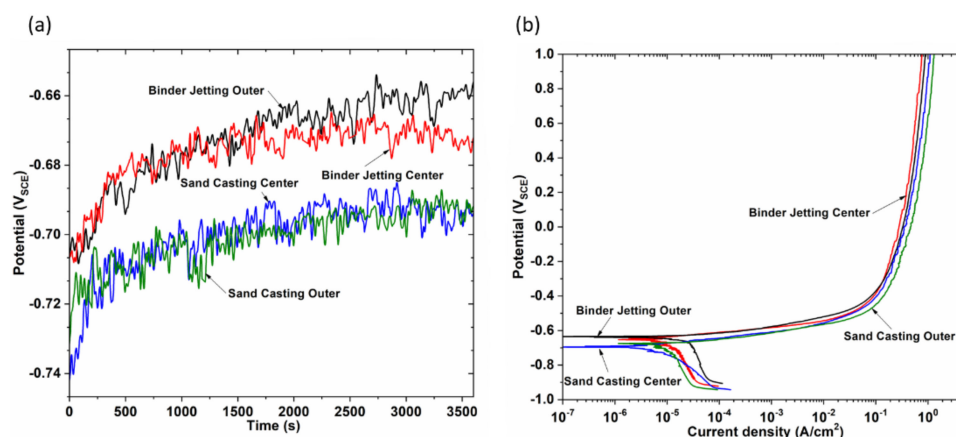
Figure 8. OCP evolution of binder jetting and of sand mold (**a**) and anodic polarization scans in the binder jetting and in the sand mold (**b**) in 3.5% NaCl, center and outer sections.

The effect of the molding on the corrosion rate of the AlSiCu alloy sample was also studied using the anodic polarization technique. Figure 8b shows the solidified potentiodynamic polarization curves for binder jetting mold and sand mold corresponding to the center and outer zones. The morphology of the curves coincides in all cases after the cathodic branch is observed; the zone of corrosion potential is slightly higher for binder jetting casting, which is consistent with the previous open circuit potential values. Then the current density increases until reaching the zone of passivity without observing in any case pitting potential, although as is known, pitting corrosion is one of the most common corrosion mechanisms in these Al alloys [40]. The curves are slightly displaced to the left for alloy solidified on the binder jetting mold, which indicates lower current density and therefore higher corrosion resistance.

Corrosion parameters such as corrosion potential (E_{corr}) and corrosion current density (i_{corr}) obtained from Tafel's analysis, are tabulated in Table 6, also included passive current density (i_{pass}) at $0.5V_{SCE}$ and polarization resistance (R_P) values. The results indicate the decrease in corrosion and passive current density with the use of binder jetting mold for the center section. However, the differences are negligible for the outer sections, which show in both cases the lowest polarization resistances. The resistance of the central section of the binder jetting casting alloy was three times higher than that obtained in the sand casting, so the kinetics of the corrosion process expressed is also substantially improved in addition to increasing thermodynamic stability with the use of the binder jetting mold.

Table 6. Electrochemical parameters estimated by Tabel method.

Sample		E_{corr} (V)	i_{corr} ($\mu A/cm^2$)	R_P (Ω/cm^2)	I_{pas} (A/cm^2)
Sand mold	Center	−0.695	90.1	289.29	0.71
	Outer	−0.683	43.0	605.54	0.90
Binder jetting mold	Center	−0.652	14.9	1752.6	0.52
	Outer	−0.643	40.5	643.31	0.61

In order to study the effect of the casting mold on the nature of the passive layer and to obtain information on the corrosion mechanisms, electrochemical impedance spectroscopy tests were carried out, which reveal greater differences between the alloys depending on the mold used in the solidification. In the Nyquist diagram (Figure 9a), a larger semi-circle is clearly observed in the binder jetting alloys, and the radius of the semi-circle is indicative of the resistance to electronic transfer and is commonly related to corrosion resistance, this coincides as shown in the Bode diagram (Figure 9b), with a higher impedance modulus in the lower frequency zone for the solidified alloy in binder jetting mold. The sample

corresponding to the outer section solidified in sand casting clearly showed the lowest corrosion resistance.
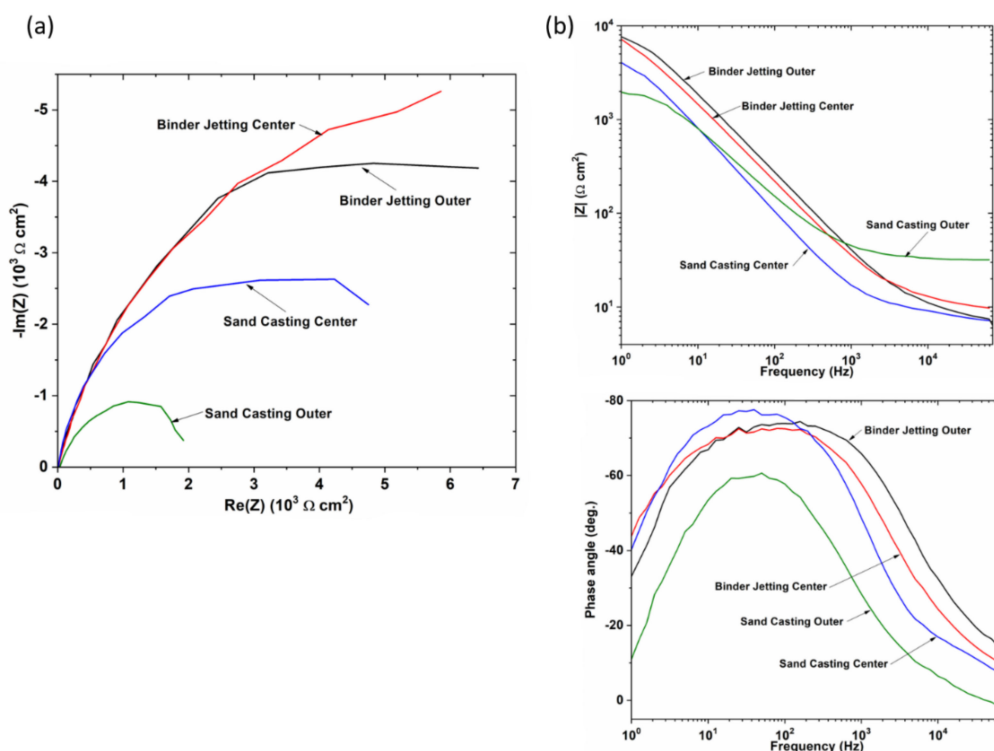

Figure 9. Nyquist (**a**) and Bode (**b**) plots of binder jetting and sand casting samples in 3.5% NaCl, center and outer sections.

The three electrochemical testing results indicate the best behavior of the samples processed by additive manufacturing mold, which must be correlated with the structural differences observed previously. From the electrochemical point of view, the most of intermetallic phases are more noble the aluminum matrix, making the alloy system highly susceptible to localized corrosion [41].

Silicon in coarse flake shapes precipitates as a consequence of the low solubility of this alloy element in the aluminum-rich matrix. Silicon is cathodic with respect to the eutectic aluminum matrix, which may lead to the formation of micro-galvanic couples. The amount of silicon [42], the morphology of silicon particles as well as the cathodic/anodic ratio [43] have important effects on galvanic corrosion between silicon and aluminum solid solution. Other microstructural features as dendrite cell size, secondary dendrite arm spacing, and grain size of aluminum phase also can affect galvanic corrosion, and it is concluded that a thicker dendritic structure tends to give the material a higher corrosion resistance compared to thinner structures where the distance between the arms is smaller [44].

The enhanced corrosion resistance of alloy solidified in the binder jetting mold compared with the alloy solidified in sand mold could be associated, in the first instance, with the reduced area ratio of eutectic silicon particles to eutectic aluminum phase [24,43] but on the other hand, with the presence of coarse silicon particles visualized in the eutectic of binder jetting alloy that can originate a lower number of micro-galvanic couples. Nevertheless, it is known that the effect of silicon is not so important due to the low corrosion current densities [34] resulting from the high polarization of silicon particles [45].

On the other hand, it is known that the presence of Fe in Al-Si-Cu alloys originates the β-Al-Fe-Si phase in the form of longer and thicker needles, with the higher the iron content and the higher the cooling speed [46]. This phase has a nobler potential than the aluminum matrix and therefore enhances the susceptibility to localized corrosion [40]. The presence of Mn resulting in α-Al-Fe-Mn-Si in the form of the so-called "Chinese

script", with lower potential reducing the galvanic corrosion compared with the β-Al-Fe-Si intermetallic phase [47]. The Fe-intermetallic compounds are more visible in outer sections of both samples, but the sample processed by sand casting had a higher amount of needles and larger size while in the sample processed by binder jetting, a greater amount of script phase was visible, it can explain the enhance corrosion behavior observed for outer ceramic casting sample. These results are in agreement with results observed by other authors [40,42,48]. These studies concluded that the iron-intermetallics compounds acted as more effective cathodes than Si on Al-Si-Cu in 3.5% NaCl solution.

Finally, the content of the Mg_2Si phase in the sample processed by binder jetting mold was higher than processed by sand one, which may enhance corrosion resistance [49] because it is anodic with respect to the aluminum matrix.

3.4. Microstructural Characterization of the Molten Samples after the Corrosion Test

After the corrosion test, a clear dissolution of phases was observed (Figure 10). The OM micrographs show that there has been a greater dissolution of the phases in the sand than in the binder jetting mold, regardless of the area studied. This may be due to the fact that the size of the phases corresponding to the sample processed by sand mold were smaller than the phase size corresponding to the samples processed by binder jetting mold.
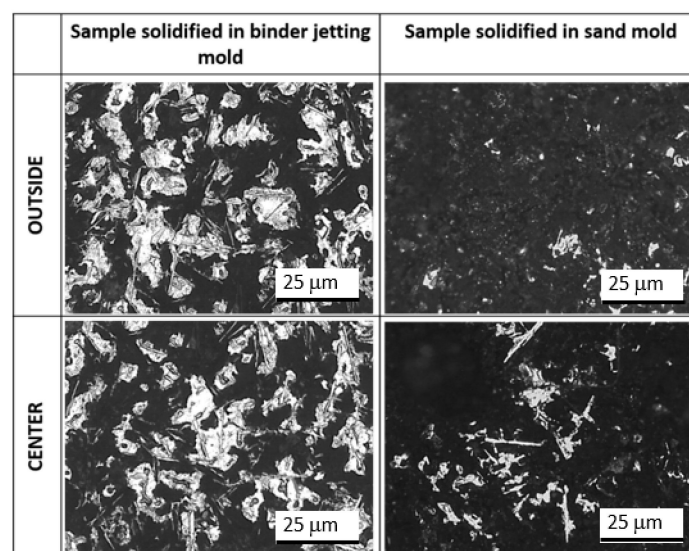

Figure 10. OM micrographs of corroded surface products immersed in 3.5% NaCl solution for the specimen in the binder jetting mold and sand casting mold.

The samples were left in the corrosive medium (3.5% NaCl) for 75 days in order to study the behavior of the oxide layer formed, as well as the effect on the existing phases. Figure 11 shows six images of an area for each sample processed with both molds (A) and (B). One of the images (SE) was derived from secondary electrons, while the other five images are high-resolution X-ray spatial distribution maps corresponding to the elements present in the SE area. The relative abundance of each element is represented by the spatial distribution of the density of dots of different colors depending on the element that is represented in each image. For both cases, there is a correlation distribution between aluminum (green image) and oxygen (red image), although in the case of the sand mold, a lower intensity and number of spots can be observed in the case of oxygen with respect to aluminum. However, in the binder jetting specimen, there is a homogeneous distribution between both elements. This could be indicative that the oxide layer formed in the sample manufactured by binder jetting is more resistant to the corrosive medium. The other elements (Si, Fe, Cu) continue to appear in the molten samples.
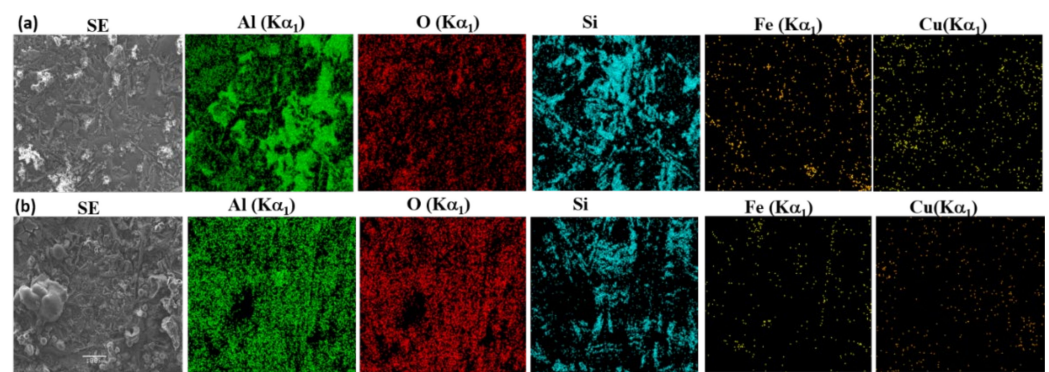
Figure 11. Element distribution mapping for Al-Si Alloy processed by sand mold (**a**) and binder jetting mold (**b**).

In order to know the number of dissolved elements after the 75 days of immersion, the concentration of the elements present in the liquid was determined by the technique of optical emission spectrometry in plasma inductively coupled.

The concentration obtained for each element after 75 days of immersion in 3.5% NaCl is presented in Table 7. In view of the results presented in the table, we can conclude that there is a greater dissolution of Al, Cu, and Si in the sample obtained with sand mold. This is in agreement with the results obtained with OM and SEM-EDX.

Table 7. Concentration (wt.%) of the elements in the 3.5% NaCl after 75 days of immersion.

Element (ppm)	Reference Material	Binder Jetting		Sand Casting	
		Center	Outer	Center	Outer
Al	<0.10	0.20	2.28	2.57	2.36
Cu	<0.01	0.03	0.06	0.20	0.04
Fe	<0.02	0.02	0.02	0.03	0.02
Mg	<0.01	0.19	0.20	0.25	0.15
Mn	<0.01	0.01	0.01	0.01	0.01
Ni	<0.02	0.02	0.02	0.02	0.02
Pb	<0.05	0.05	0.05	0.05	0.05
Si	<0.10	0.28	0.32	0.51	0.34
Sn	<0.10	0.10	0.10	0.10	0.10
Ti	<0.01	0.01	0.01	0.01	0.01
Zn	<0.02	0.02	0.08	0.33	0.02

4. Conclusions

The present study is directed to investigate the influence of two different molds on the microstructure and corrosion behavior of an aluminum alloy. The major conclusions are:

The corrosion behavior depends on the mold, but it is irrespective of the aluminum cast zone.

The OCP results revealed the formation of the passive layer for the alloy processed with the two molds. Although the slightly higher potentials in OCP, the lower current densities in the PA test, as well as the decrease in corrosion and passive current density in the Tafel test obtained for samples processed by additive manufacturing, reveal that in this case, the aluminum alloy is more corrosion-resistant.

The variation of corrosion behavior with both molds is related to the differences found in the microstructure. The binder jetting-processed alloy microstructure shows galvanic pairs of silicon and α-Al-Fe-Mn-Si intermetallic precipitates that limit corrosion resistance. While with the sand mold, the microstructure is rich in needle-like intermetallic compounds (β-Al-Fe-Si) that make corrosion accelerate.

References

1. Yılmaz, M.S.; Özer, G.; Öter, Z.C.; Ertugrul, O. Effects of hot isostatic pressing and heat treatments on structural and corrosion properties of direct metal laser sintered parts. *Rapid Prototyp. J.* **2021**, *27*, 1059–1067. [CrossRef]
2. Cohen, A.L. From rapid prototyping to the second industrial revolution. In Proceedings of the Third International Conference on Rapid Prototyping, Dayton, OH, USA, 23–25 June 1992; pp. 189–192.
3. Low, Z.X.; Chua, Y.T.; Ray, B.M.; Mattia, D.; Metcalfe, I.S.; Patterson, D.A. Perspective on 3D printing of separation membranes and comparison to related unconventional fabrication techniques. *J. Membr. Sci.* **2017**, *523*, 596–613. [CrossRef]
4. Attar, M.; Aydin, S.; Arabaci, A.; Mutlu, I. Mechanical meta-material-based polymer skin graft production by rapid prototyping and replica method. *Rapid Prototyp. J.* **2021**, *27*, 278–287. [CrossRef]
5. Wang, J.; Sama, S.R.; Manogharan, G. Re-Thinking Design Methodology for Castings: 3D Sand-Printing and Topology Optimization. *Int. J. Met.* **2019**, *13*, 2–17. [CrossRef]
6. EPA (Environmental Protection Agency). *Profile of the Metal Casting Industry*; Office of Compilance Sector Notebook Project; EPA (Environmental Protection Agency): Washington, DC, USA, 1997.
7. Tang, Y.; Huang, Z.; Yang, J.; Xie, Y. Enhancing the Capillary Force of Binder-Jetting Printing Ti6Al4V and Mechanical Properties under High Temperature Sintering by Mixing Fine Powder. *Metals* **2020**, *10*, 1354. [CrossRef]
8. Mariani, M.; Goncharov, I.; Mariani, D.; De Gaudenzi, P.G.; Popovich, A.; Lecis, N.; Vedani, M. Mechanical and microstructural characterization of WC-Co consolidated by binder jetting additive manufacturing. *Int. J. Refract. Met. Hard Mater.* **2021**, *100*, 105639. [CrossRef]
9. Cheng, Y.-L.; Tseng, T.-W. Study on driving waveform design process for multi-nozzle piezoelectric printhead in material-jetting 3D printing. *Rapid Prototyp. J.* **2021**, *27*, 1172–1180. [CrossRef]
10. Cheng, Y.-L.; Chang, C.-H.; Kuo, C. Experimental study on leveling mechanism for material-jetting-type color 3D printing. *Rapid Prototyp. J.* **2020**, *26*, 11–20. [CrossRef]
11. Li, J.; Yan, R.; Yang, Y.; Xie, F. Water-based binder preparation and full-color printing implementation of a self-developed 3D printer. *Rapid Prototyp. J.* **2021**, *27*, 530–536. [CrossRef]
12. Snelling, D.; Li, Q.; Meisel, N.; Williams, C.B.; Batra, R.C.; Druschitz, A.P. Lightweight Metal Cellular Structures Fabricated via 3D Printing of Sand Cast Molds. *Adv. Eng. Mater.* **2015**, *17*, 923–932. [CrossRef]
13. Walker, J.; Harris, E.; Lynagh, C.; Beck, A.; Lonardo, R.; Vuksanovich, B.; Thiel, J.; Rogers, K.; Conner, B.; MacDonald, E.; et al. 3D Printed Smart Molds for Sand Casting. *Int. J. Met.* **2018**, *12*, 785–796.
14. George, S.; Roy, A.; McKenna, N.; Singamneni, S.; Diegel, O.; Singh, D.; Neitzert, T.; St George, J.; Roy Choudhury, A.; Yarlagadda, P. Direct Metal casting through 3D printing: A critical analysis of the mould characteristics. In Proceedings of the 9th Global Congress on Manufacturing and Management (GCMM2008), Gold Coast, QLD, Australia, 12–14 November 2008; pp. 1–5.
15. Vaezi, M.; Chua, C.K. Effects of layer thickness and binder saturation level parameters on 3D printing process. *Int. J. Adv. Manuf. Technol.* **2011**, *53*, 275–284. [CrossRef]
16. Garzón, E.O.; Alves, J.L.; Neto, R.J. Study of the viability of manufacturing ceramic moulds by additive manufacturing for rapid casting. *Ciência Tecnologia Materiais* **2017**, *29*, e275–e280. [CrossRef]
17. Snelling, D.A.; Williams, C.B.; Druschitz, A.P. Mechanical and material properties of castings produced via 3D printed molds. *Addit. Manuf.* **2019**, *27*, 199–207. [CrossRef]
18. Snelling, D.; Blount, H.; Forman, C.; Ramsburg, K.; Wetzel, A.; Williams, C.; Druschitz, A. The Effects of 3D Printed Molds on Metal Castings. In Proceedings of the Solid Freeform Fabrication Symposium, Austin, TX, USA, 12–14 August 2013; pp. 827–845.
19. Barresi, J.; Kerr, M.J.; Wang, H.; Couper, M.J. Effect of magnesium, iron and cooling rate on mechanical properties of Al-7Si-Mg foundry alloys. *AFS Trans.* **2000**, *108*, 563–570.
20. Szklarska-Smialowska, Z. Pitting corrosion of aluminum. *Corros. Sci.* **1999**, *41*, 1743–1767. [CrossRef]
21. Guo, W.; Li, J.; Qi, M.; Xu, Y.; Ezatpour, H.R. Effects of heat treatment on the microstructure, mechanical properties and corrosion resistance of AlCoCrFeNiTi0.5 high-entropy alloy. *J. Alloys Compd.* **2021**, *884*, 161026. [CrossRef]

22. Davis, J.R. *Alloying: Understanding the Basics*; ASM International: Metals Park, OH, USA, 2001; p. 647.

23. Fadavi Boostani, A.; Tahamtan, S. Fracture behavior of thixoformed A356 alloy produced by SIMA process. *J. Alloys Compd.* **2009**, *481*, 220–227. [CrossRef]

24. Tahamtan, S.; Fadavi Boostani, A. Evaluation of pitting corrosion of thixoformed A356 alloy using a simulation model. *Trans. Nonferrous Met. Soc. China* **2010**, *20*, 1702–1706. [CrossRef]

25. Ye, H. An overview of the development of Al-Si-alloy based material for engine applications. *J. Mater. Eng. Perform.* **2003**, *12*, 288–297. [CrossRef]

26. Chen, C.L.; West, G.D.; Thomson, R.C. Characterisation of Intermetallic Phases in Multicomponent Al-Si Casting Alloys for Engineering Applications. *Mater. Sci. Forum* **2006**, *519*, 359–364. [CrossRef]

27. Donatus, U.; Thompson, G.E.; Omotoyinbo, J.A.; Alaneme, K.K.; Aribo, S.; Agbabiaka, O.G. Corrosion pathways in aluminium alloys. *Trans. Nonferrous Met. Soc. China* **2017**, *27*, 55–62. [CrossRef]

28. Li, J.; Dang, J. A summary of corrosion properties of Al-Rich solid solution and secondary phase particles in al alloys. *Metals* **2017**, *7*, 84. [CrossRef]

29. Couture, A. Iron in aluminium casting alloys—a literature survey. *AFS Int. Cast Met. J.* **1981**, *6*, 9–17.

30. Crepeau, P.N. Effect of Iron in Al-Si Casting Alloys A Critical Review. *AFS Trans.* **1995**, *103*, 361–366.

31. Cao, X.; Campbell, J. Morphology of β-Al$_5$FeSi Phase in Al-Si Cast Alloys. *Mater. Trans.* **2006**, *47*, 1303–1312. [CrossRef]

32. Castro-Sastre, M.A.; Fernández-Abia, A.I.; Rodríguez-González, P.; Martínez-Pellitero, S.; Barreiro, J. Characterization of materials used in 3D-printing technology with different analysis techniques. *Ann. DAAAM Proc.* **2018**, *29*, 947–954.

33. ASTM International. *ASTM G-5-87, Standard Reference Test Method for Making Potentiostatic and Potentiodynamic Anodic Polarization Measurements*; ASTM International: West Conshohocken, PA, USA, 1993.

34. Bonsack, W. Effects of minor alloying elements on aluminium casting alloys: Part II. Aluminum–silicon alloys. *ASTM Bull.* **1943**, *124*, 41–51.

35. Liu, J.; Xiu, Z.; Liang, X.; Li, Q.; Hussain, M.; Qiao, J.; Jiang, L. Microstructure and properties of Sip/Al-20 wt.% Si composite prepared by hot-pressed sintering technology. *J. Mater. Sci.* **2014**, *49*, 1368–1375. [CrossRef]

36. Bonatti, R.S.; Siqueira, R.R.; Padilha, G.S.; Bortolozo, A.D.; Osório, W.R. Distinct Alp/Sip composites affecting its densification and mechanical behavior. *J. Alloys Compd.* **2018**, *757*, 434–447. [CrossRef]

37. Bonatti, Y.A.; Bortolozo, A.D.; Costa, D.; Osório, W.R. Morphology and size effects on densification and mechanical behavior of sintered powders from Al-Si and Al-Cu casting alloys. *J. Alloy. Compd.* **2019**, *786*, 717–732. [CrossRef]

38. Tash, M.M.; Mahmoud, E.R.I. Development of in-Situ Al-Si/CuAl$_2$ metal matrix composites: Microstructure, hardness, and wear behavior. *Materials* **2016**, *9*, 442. [CrossRef] [PubMed]

39. Drouzy, M.; Richard, M. Effet des conditions de solidification sur la qualité des alliage de fonderie de A-U5 GT et A-S7 G, estimation des caractéristiques mécaniques. *Fonderie* **1969**, *285*, 49–56.

40. Arrabal, R.; Mingo, B.; Pardo, A.; Mohedano, M.; Matykina, E.; Rodríguez, I. Pitting corrosion of rheocast A356 aluminium alloy in 3.5 wt.% NaCl solution. *Corros. Sci.* **2013**, *73*, 342–355. [CrossRef]

41. Jain, S. *Corrosion and Protection of Heterogeneous Cast Al-Si (356) and Al-Si-Cu-Fe (380) Alloys by Chromate and Cerium Inhibitors*; The Ohio State University: Columbus, OH, USA, 2006.

42. Osório, W.R.; Goulart, P.R.; Garcia, A. Effect of silicon content on microstructure and electrochemical behavior of hypoeutectic Al-Si alloys. *Mater. Lett.* **2008**, *62*, 365–369. [CrossRef]

43. Tahamtan, S.; Boostani, A.F. Quantitative analysis of pitting corrosion behavior of thixoformed A356 alloy in chloride medium using electrochemical techniques. *Mater. Des.* **2009**, *30*, 2483–2489. [CrossRef]

44. Oztürk, I.; Agaoglu, G.H.; Erzi, E.; Dispinar, D.; Orhan, G. Effects of strontium addition on the microstructure and corrosion behavior of A356 aluminum alloy. *J. Alloys Compd.* **2018**, *763*, 384–391. [CrossRef]

45. Davis, J.R. *ASM Specialty Handbook: Aluminum and Aluminum Alloys*; ASM International: Metals Park, OH, USA, 1993.

46. Kucharikóvá, L.; Liptáková, T.; Tillová, E.; Kajánek, D.; Schmidová, E. Role of chemical composition in corrosion of aluminum alloys. *Metals* **2018**, *8*, 581. [CrossRef]

47. Samuel, A.M.; Doty, H.W.; Valtierra, S.; Samuel, F.H. βAl$_5$FeSi phase platelets-porosity formation relationship in A319.2 type alloys. *Int. J. Met.* **2018**, *12*, 55–70.

48. Mingo, B.; Arrabal, R.; Pardo, A.; Matykina, E.; Skeldon, P. 3D study of intermetallics and their effect on the corrosion morphology of rheocast aluminium alloy. *Mater. Charact.* **2016**, *112*, 122–128. [CrossRef]

49. Yasakau, K.A.; Zheludkevich, M.L.; Lamaka, S.V.; Ferreira, M.G.S. Role of intermetallic phases in localized corrosion of AA5083. *Electrochim. Acta.* **2007**, *52*, 7651–7659. [CrossRef]